Graphical abstract

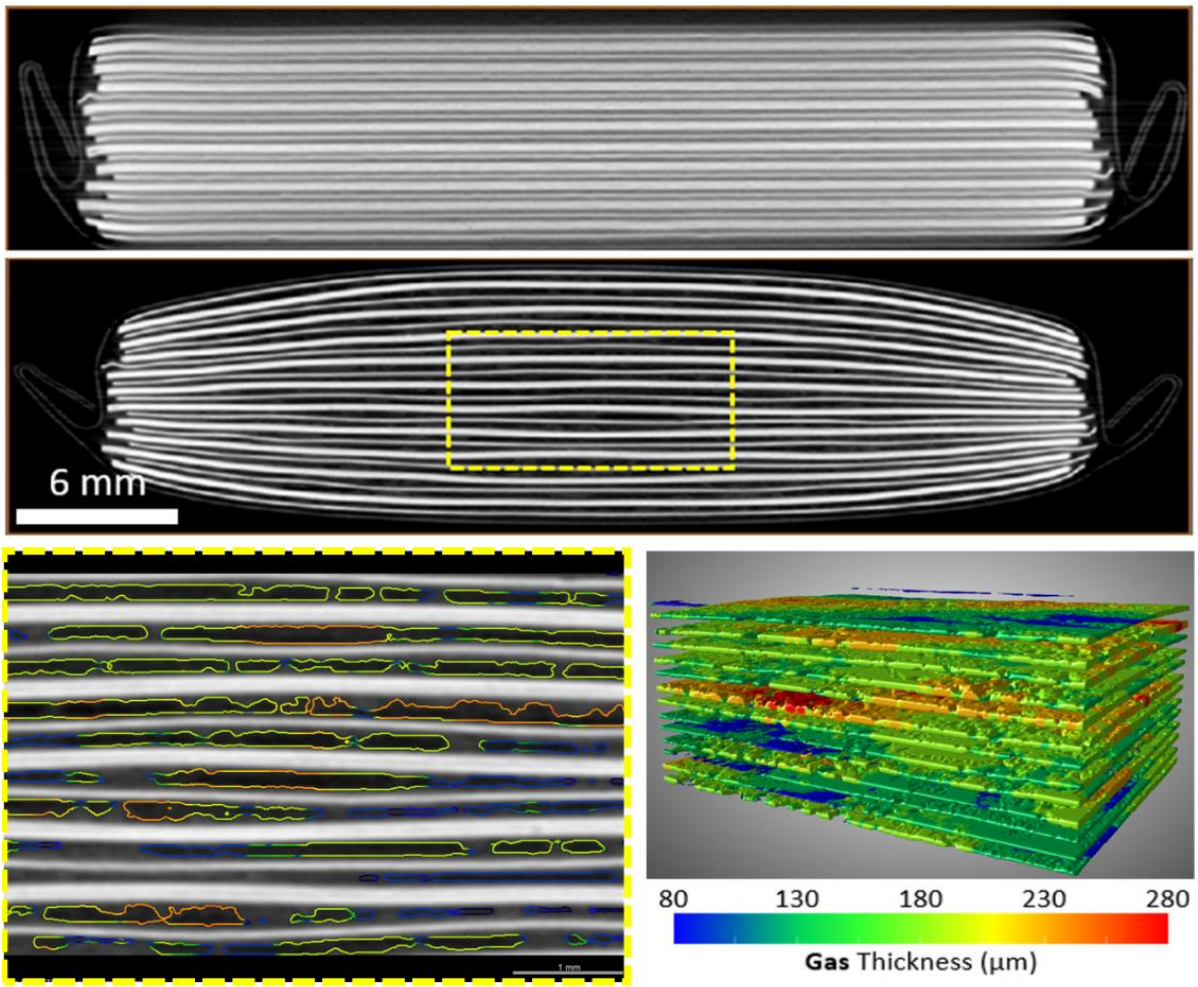

In-situ X-ray tomographic imaging study of gas and structural evolution in a commercial Li-ion pouch cell

Wenjia Du[1, 2], Rhodri E. Owen[1, 2], Anmol Jnawali[1, 2], Toby P. Neville[1], Francesco Iacoviello[1], Zhenyu Zhang[1, 2], Sebastien Liatard[3], Daniel J. L. Brett[1, 2], Paul R. Shearing[1, 2*]

1. Electrochemical Innovation Lab, Department of Chemical Engineering, University College London, London, WC1E 7JE, UK.
2. The Faraday Institution, Quad One, Harwell Science and Innovation Campus, Didcot OX11 0RA, UK.
3. OXIS Energy Ltd, E1 Culham Science Centre, Abingdon, Oxfordshire, OX14 3DB, UK

Keywords: Li-ion pouch cell, cycling, X-ray computed tomography, gas evolution, thickness

Corresponding Author: Paul Shearing (p.shearing@ucl.ac.uk)

Abstract

Gas generation within Li-ion batteries (LIB) leads to an increase in resistance, thereby, reducing their cycle lifetime. The chance of catastrophic failure *via* internal gas evolution may increase as a function of cell size and capacity. However, *in-situ* studies of gas evolution at the cell level are very limited due to limited number of techniques that can effectively probe this. Hence, for the first time, we employed high-energy X-ray tomography to non-destructively observe the structural evolution (gas and electrodes) as a function of cycle numbers for a 400 mAh commercial Li-ion pouch cell. Gas agglomeration led to cell deformation in different areas were observed in 4D (3D+time), the subsequent quantification including the volume fraction, surface area and thickness shows a heterogeneous gas distribution, revealing the degradation mechanism involving the coalescence of gas. This study demonstrates a feasible case of the use of lab-based X-ray to investigate the cell degradation and monitor state of health (SOH) by tracking the thickness *in-situ*, and provides practical guidance for designing safer pouch cells.

1. Introduction

Rechargeable lithium-ion batteries (LIBs) are widely considered as the most competitive solution for electric vehicles (EVs) [1, 2]. Nowadays, affordable LIBs with high durability, fast charging and high capacity are required. The energy and power densities of LIBs have significantly increased since the first Li-ion battery was commercialised in 1980s [3]. However, safety issues persist which restrict the full practical utilisation of LIBs [4]. Particularly, the generation of gas within sealed batteries at extreme conditions (i.e., high C-rate [5], higher temperature [6] and over potential, etc.) may lead to detrimental effects, distorting the cell structures (delamination), reducing life time, and even causing thermal runaway [7].

To date, extensive research has been carried out to understand gas evolution across different length and/or time scales using multi-modal characterisations [8]. In general, these investigations could be divided into two main categories: gas chromatography mass spectrometry (GC–MS) and imaging observations. On the one hand, by GC-MS, the analysis of gas chemical compositions and quantities were carried out to understand the voltage-dependent electrolyte consumption [6, 9]. For instance, gaseous products (H_2, CO, CO_2, O_2, CH_4, C_2H_4, and C_2H_6) from the decomposition of solvents in contact with the negative electrode during cell operation has been identified [10]. The disadvantage of the GC–MS approach is that the custom-made cell designs usually require a high excess of electrolyte. On the other hand, the direct measurement of exterior pouch cell thickness change at different state of charge (SOC) have been typically conducted by optical imaging with digital image correlation (DIC), allowing researchers to correlate displacement with internal gas-induced stress (and strain) [11-14]. Studies have shown that there is an overall trend for the cell to become thicker as it ages and this may suggest using the thickness as one of metrics to

monitor the SOH and detect gas-induced bulging [15]. Unfortunately, it is not possible using above techniques to understand what happens inside the cell during cell operation and the dominant factor which leads to the thickness increment. The internal structure evolution is so far, not well understood. To visualise the internal structure, advanced imaging techniques have been utilised. Neutron imaging possesses the advantage of tracking distribution of lithium (Li) and hydrogen (H) to correlate gas evolution during cell operation in the 2D plane [16-21]. However, the limited spatial and temporal resolution may not well resolve the cell architecture in 3D. To complement neutron imaging, lab-based X-ray tomographic imaging has been used to capture the 3D displacement of electrode assemblies in pouch cell [22]. The development of 3rd generation light sources facilitated 4D *real-time* dynamic investigations [23]. For instance, the gas formed from the Si electrode in a Swagelok was observed *in situ* [24], rationalizing the gassing mechanism at sub-micron scale. Very recently, *operando* electrochemical acoustic [25-27] time-of-flight was coupled with fast synchrotron X-ray radiography to provide a new understanding of gas-induced deformation during thermal abuse [28]. However, the aforementioned investigations are mainly focused on either different cell configurations or time-dependent information in a 2D plane or limited to a single discharge-charge cycle.

Herein, we demonstrate that *in-situ* X-ray tomographic imaging provides both qualitative and quantitative information about the evolution of gas and electrodes in a commercially available, functional Li-ion pouch cell. For the first time, the time-lapse 3D thickness distribution at different regions of interest (ROIs) provides an opportunity to track the non-uniform gas evolution as a function of cycle number. This work demonstrated the application of lab-based, high energy X-ray tomography to observe internal cell architectures in 4D at the macro-scale (resolution of $\sim 23\ \mu m$). This study not only provides practical guidance for

designing next-generation, high-energy and high-power density LIBs for EVs, we also developed a fast approach to inspect the cell state of health (SOH) for potential second-life use by developing a robust model to accurately evaluate the cell thickness change and the corresponding gas volume. 3D imaging of the pouch cell is freely accessible *via* the University College London (UCL) Research Data Repository for battery simulations.

2. Experimental Methods

2.1 Electrochemical measurements

A commercial Li-ion pouch cell composed of a $LiCoO_2$ (LCO) cathode with a graphite anode (PL-402248-2C, 400 mAh, AA Portable Power Corp, USA) was examined by X-ray tomography to understand the structural changes (at the electrode-to-cell level) as a function of the cycle number. The cell (dimension: 49 × 22.5 × 4.1 mm^3) was cycled at constant current of 200 mA (0.5 C-rate) from 2.75 V to 4.2 V using a GAMRY 1000E potentiostat (GAMRY Instruments, USA). A voltage was hold at 4.2 V after the charging period until the current dropped below 2 mA. The cell was scanned at various points in its cycle life: pristine, and at the 100^{th}, 150^{th} and 200^{th} cycle as shown in Fig. 1b. After galvanostatic cycling, X-ray imaging was carried out at the nominal voltage (3.75 V): all parameters of electrochemical measurement are summarised in Table 1.

Electrochemical Impedance Spectroscopy (EIS) measurements were performed on identical LCO pouch cells after the 20^{th} and 150^{th} cycles by applying an alternate voltage signal with an amplitude of 10 mV within frequency ranging from 1 MHz to 0.1 Hz. The associated EIS spectra was analysed and fitted using the GAMRY Echem Analyst (Fig. 1c and Table 2).

2.2 Post-mortem characterisation

Another Li-ion cell was dissembled after 50 cycles in an Ar-filled glove box for further SEM and EDX analysis to confirm the electrode chemistry using a Zeiss EVO MA10 SEM (Carl Zeiss AG, Germany) coupled with a AztecONE detector (Oxford Instruments, Oxford, UK). The thickness of electrodes was physically measured by a digital thickness gauge (Mitutoyo, Japan) to validate X-ray measurements.

2.3 In-situ X-ray computed tomography (CT) and imaging processing

Time-lapse X-ray imaging of the pouch cell was performed on a Nikon XTH 225 (Nikon Metrology, UK) using a tungsten target and a 0.5 mm Cu filter. The experimental setup is show in Fig. S1a. The bespoke cell holder (Fig. S1b) was fabricated by a 3D printer (Ultimaker, US) to accommodate the small Li-ion pouch cell. All scans of the cell (including the cell in pristine and cycled states) were carried out under the same X-ray conditions: 140 kV voltage, 65 µA current, and 9.1 W power. For each tomographic dataset, 2089 projections were obtained with an exposure time of 1 second per projection. The entire pouch cell was maintained within the field of view (FOV) to obtain a spatial resolution with voxel size of 23 µm. The details of the X-ray tomographic acquisition parameters are summarised in Table 3.

The raw X-ray projections were reconstructed using Nikon CT Pro 3D software (Version XT 4.4.4, Nikon Metrology, Tring, UK). The centre of rotation was calculated automatically and a beam hardening correction was applied during reconstruction. The reconstructed micro-CT datasets were interactively imported into Spyder (an open-source python platform), Avizo

2019.4 (Thermo Fisher Scientific, UK) and Dragonfly (ORS, Montreal, Canada) for further denoising, segmentation, visualization, and quantification. Specifically, three regions (denoted: top, middle and bottom in Fig. S2) in each scan of the sample were manually extracted from the entire 3D volume. After cropping non-informative regions to reduce processing time, an un-sharp filter was applied to sub-volume datasets to remove the noise. The sub-volume datasets were automatically batch segmented in Spyder using the multi-Otsu algorithms [29]. Also, the binary segmentation was applied to these denoised sub-volume datasets before the thickness calculation. This approach is fast, robust and reproduceable. As an example, a 2D thickness measurement of gas structure after 200th cycle is presented in Fig. S3. Similar method was applied to the electrode layers.

3. Results and discussion

To investigate the correlation between the Li-ion pouch cell's electrochemical performance and its structure at the cell level, X-ray image acquisitions were performed at regular intervals during galvanostatic cycling. The charge-discharge voltage profiles, in the voltage range of 2.75 and 4.25 V, at 0.5C for up to 200 cycles are shown in Fig 1a. This large voltage window was recommended by the cell manufacturer. However, we accelerate the degradation process by eliminating the rest stage between cycles. Correspondingly, Fig 1b shows the cycling performance of the cell. The cell shows similar initial charge and discharge capacities of ~ 425 mA h which is slightly higher than the manufacturer's reported value of 400 mA h. After 50 cycles, the capacity retention decreases to ~80 % (~340 mA h) and the Coulombic efficiency is maintained at ~97%.

The Nyquist plots in Fig. 1c exhibit a medium frequency semicircle and a low frequency tail, which could be fitted to intrinsic resistance (R_i), charge transfer resistance and constant phase element from both the anode side (R_{c1}, Q_1) and cathode side (R_{c2}, Q_2), and Warburg diffusion resistance (W), as shown in the equal circuit inset of Fig. 1c. It revealed that both the charge transfer resistances from anode and cathode side are increasing as the cell cycles (0.5 C), leading to the increased total charge transfer resistance from 0.37 Ω at 20th cycle to 0.46 Ω at 150th cycle (Table 2). The increase of the cell resistance may likely be associated with the degradation of electrode materials and gas generation which will be discussed later.

3D volume rendering of the CT images of the pristine cell and after the 200th cycle is presented in Figs. 1e-f, along with respective 2D cross-section slices in Figs. 1g-h. The segmented electrode layers in green are superimposed on 3D volumes to highlight the cell architecture. At the 200th cycle, the cell has undergone significant volume expansion, which can be clearly observed both from the visible photographs (Fig. 1d) and the CT image (Fig. 1f). Such expansion was caused by pressure build-up as a result of gas generation, which has been observed in [22]. We minimize the age-induced expansion as the cell was scanned immediately after cycling. Non-destructive CT technique has no influence on battery performance (using this combination of X-ray source and imaging parameters), we are therefore able to evaluate the cell degradation by tracking gas evolution in a cell at various stages of its lifetime. The pristine cell (Fig. 1g) has parallel electrode assemblies (electrode and Cu current collector), showing uniform cell spacings (average of 55 µm). While the cycled sample demonstrates buckling of the electrode assembly, along with non-uniform electrode spacing (Fig. 1h), indicating major degradation of the internal architecture. The bulk deformation was more prominent in the central region of the cell whereas both ends remained tightly stacked. The cell deformation ratio ($\sigma = \Delta L/L = (L_{x\,cycle} - L_{pristine}) / L_{pristine,}\, x = 1$,

2, … n denoted cycle number) at the most severe area could be determined *via* measuring the largest change of exterior thickness (*L*) as plotted in Fig. 4a. These thicknesses increase from 4000 to 6900 µm after the 200th cycle, resulting in a total swelling at X-Y plane reached ~72.5 % ($\sigma_{200th\ cycle} = (L_{200th\ cycle} - L_{pristine}) / L_{pristine}$).

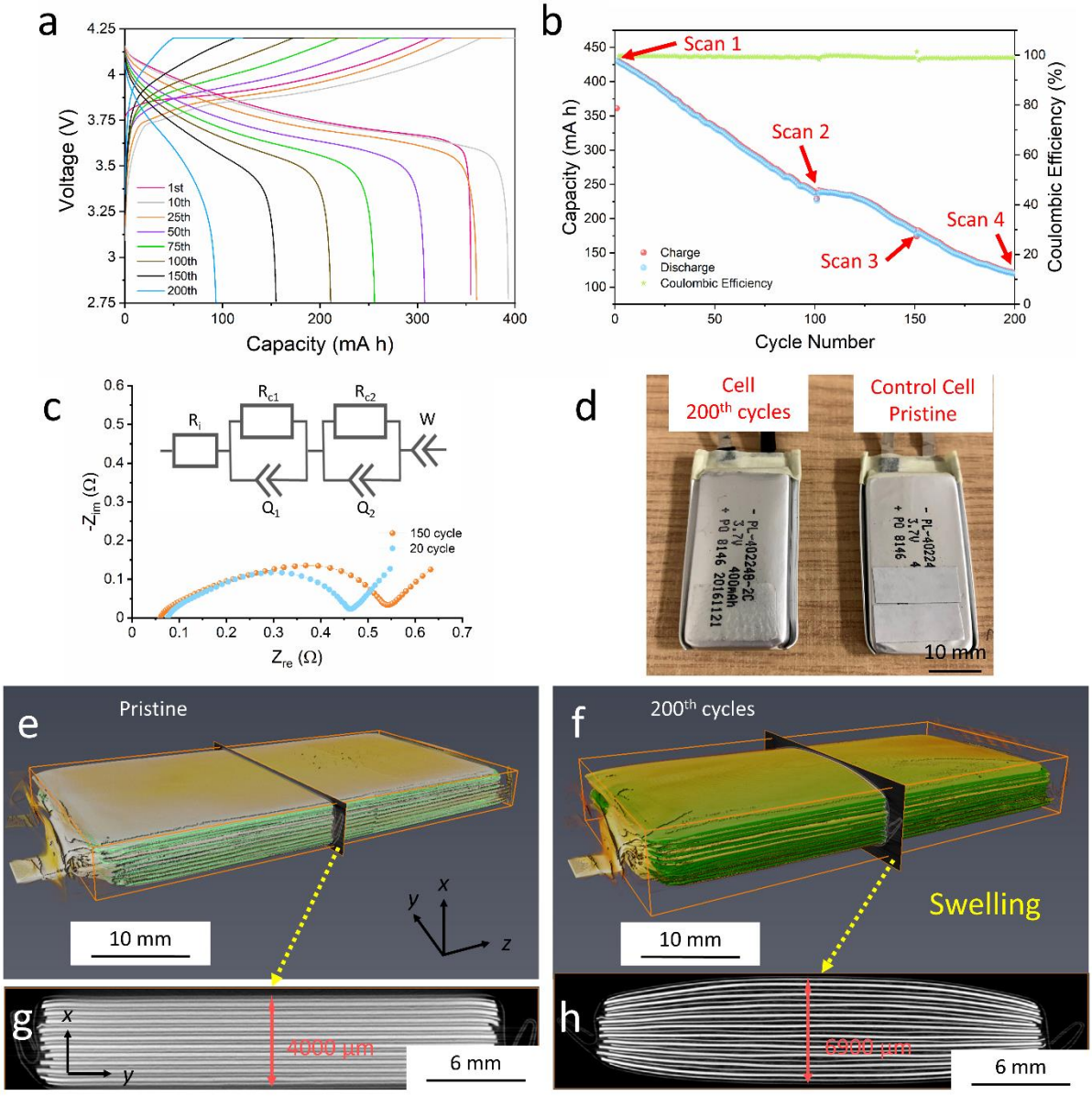

Fig. 1. The room temperature (25 ˚C) electrochmical measurements: (a) the charge-discharge profiles of various cycles (voltage range of 2.75–4.25 V, 1st, 10th, 25th, 50th, 75th, 100th, 150th, and 200th) at a rate of 0.5 C, and (b) the cycling performance for 200 cycles. (c) EIS measurements of the Li-ion pouch cell upon cycling at 0.5 C rate at room temperature, the Nyquist plots are presented for 20th and 150th cycles respectively. (d) The genuine images of the 200th cycles (left) and fresh (right) cells. 3D volume rendering of entire cells and their respective 2D cross-section slices at (e, g) pristine state and (f, h) after 200 cycles. The segmented cathode layers (green) are superimposed with their 3D volumes to highlight the deformation. It should be noted that X-ray tomograms are obtained after the cell is measured at its nominal voltage of 3.75 V.

In Fig. 2, after cycling, gas generation and evolution in 2D slice was directly observed by using *in-situ* X-ray CT due to the negligible attenuation caused by the gas. In Fig. 2k, both 1st and 2nd greyscale intensity peaks shift to the lower threshold region (< 65), with intensities gradually increasing, confirming the continuous generation of gas in successive cycles. At the pristine state, a lower gas content may be present in the cell as expected, however, after the 100th cycle, the electrolyte gradually decomposed by reacting with graphite anode [30] resulting in the production of gas, which accumulated as the black regions observed (Figs. 2b). The gas cavity is too small to be verified in the pristine state, therefore we displayed the gas after 100 cycles. We found the gas distribution was non-uniform at the macro-scale (cell level). Such heterogeneous phenomena has been observed in microscale configurations (particle level) [24]. After the 200th cycle, gas became more pronounced due to the continuous reduction of the electrolyte, resulting in the isolated particle-like structures (Figs. 2d & e) in the FOV. All labelled Images (Figs. 2c, e, h & j) were segmented from raw images (Figs. 2b, d, g & i) using the Otsu method [29].

It is unclear if the gas originated from the reaction at interface between the electrodes and surrounding electrolyte at resolution of 23 micron, but it is possible to follow the gas evolution at certain cycling states by time-lapse X-ray imaging (Fig. 2), strengthening the previous studies [8]. The procedure as follow; Firstly, some cavities (which act as 'nucleation' point for the gas bubble) may already be presented in the periphery of the electrode and Cu current collector, and grow into gas bubbles. Next, smaller volume gas bubbles merged into the larger agglomerations (Fig. 2g). Eventually, the electrolyte will be largely consumed and replaced by the plate-like gas channels inserted between the stack electrode layers (Fig. 2j). This leads to a severe displacement of electrodes (Fig. 2j), cell resistance increase (Fig. 1c) and capacity fading (irreversible drops from ~425 to ~120 mA h as shown in Fig. 1b).

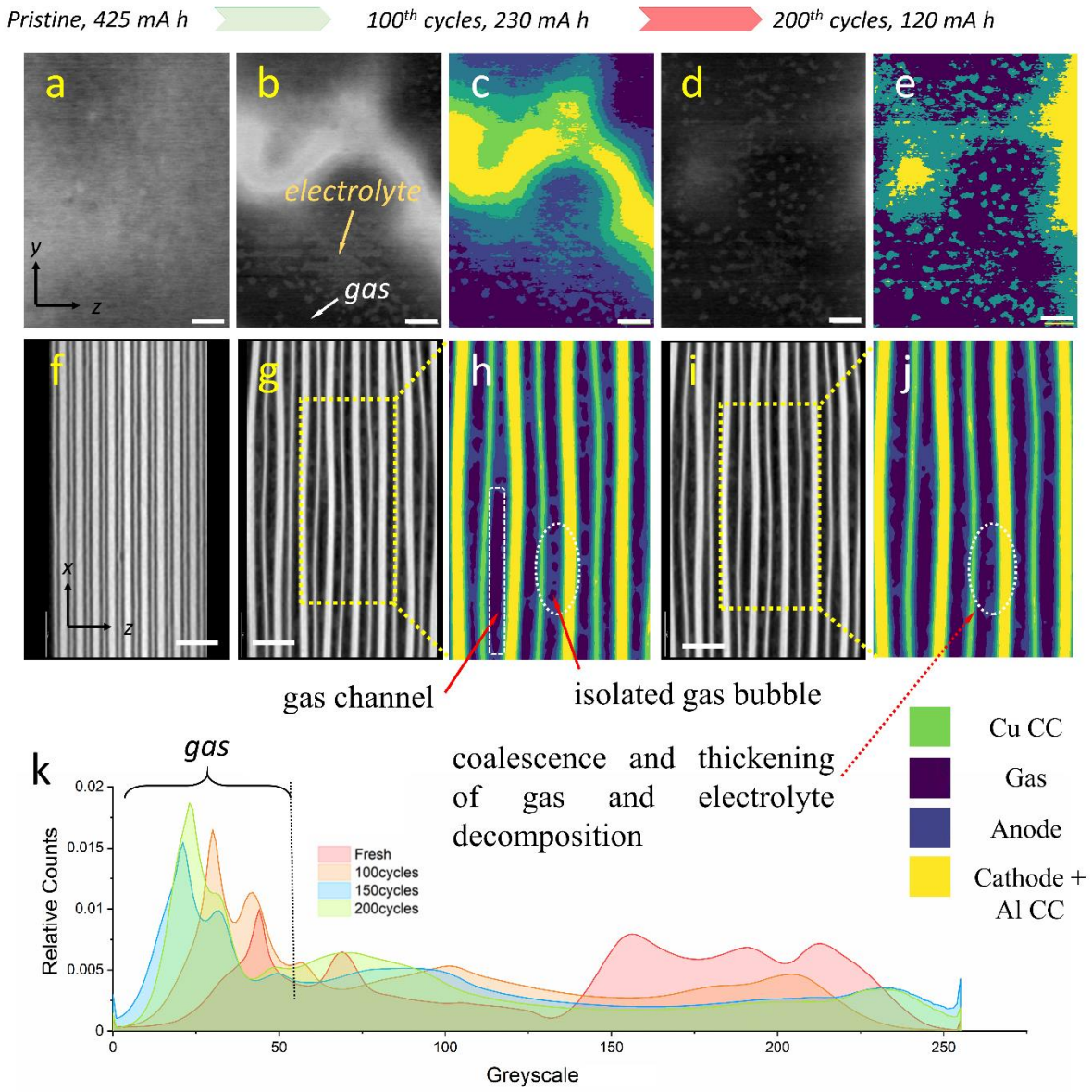

Fig. 2. Time-lapse X-ray tomographic slices of polymer Li-ion pouch cell at the (a, f) pristine, (b, c, g, h) 100th, and (d, e, i, j) 200th cycles, showing the gas evolution and correlative cell deformation. Three sub-volumes (300 × 180 × 400 voxels), included the (a-e) front and (f-j) side view of slices, are extracted from the entire cell volume at the same location. The gas formation, agglomeration, and thickening at mesoscale are highlighted in the enlarge ROI at 100th (h) and 200th (j) cycle. Both images (h & j) are segmented for (g, i) respectively using the multiple Otsu method. The image segmentations (c, e, h, & j) show four labelled phases (green: Cu current collector, yellow: doube cathode layer with Al current collector, blue: electrolyte, and purple: gas). (k) The overlapped X-ray imaging grayscale histograms of the same cell before and after various cycle numbers. Scale bars are 1 mm for (a-e, f-g, and i).

To closely visualize 3D structure and minimize the computational effort, three sub-volumes were extracted from the entire tomographic volume at various points in its cycle life. In Fig.

3, we demonstrated 4D macro-structures of the gas (left column) and electrode (right column) before and after cycling at the middle and top regions. Fig. S1 shows where sub-regions are selected. It should be noted that (1) SEM and EDX results (Fig. S4) confirm that each 'electrode layer' included a double-layer LCO cathode or graphite anode coated on both side of an aluminium or a copper current collector; (2) the LCO cathodes were selected for visualisation because of high X-ray attenuation; (3) Fig. 3 shows the morphologies of the electrodes together with its thickness distribution (assigned different colours) under various conditions. Figs. 3a-c show the 3D morphology of the evolving gas structure in the middle region (Region (ii) in Fig. S2), in which each layer has been coloured by its local thickness (and other phases have been deliberately removed). At the 100th cycle, there are some unconnected areas and a large number of grooves on the gas structure (Fig. 3a), indicating less gas has been produced at that location. While, after the 200th cycle in Fig. 3c, these grooves are largely disappeared and layer-like structure become more obvious (isolated gas bubbles join together, grooves on the surface of gas channels have been filled), suggesting more gas has been generated due to electrolyte consumption. Indeed, Fig. 4c shows that the volume fraction of gas ($V_{gas\text{-}mid}$), from the 100th to 200th cycles, had almost doubled (increased from 15.28 to 29.9 %). In addition, the volume specific gas surface area ($S_{gas\text{-}mid}$) decreased from 0.033 to 0.022 µm^2/µm^3 (Fig. 4d), proving the evidence of gas agglomeration. We speculate that formation of a large amount of gas will lead to delamination of electrode layers which increases the cell resistance, because the electrolyte will be replaced by non-conductive gas when the cell swells; the above EIS and CT results support this assumption. In fact, the above gassing phenomenon suggests that the integrity of individual gas layer will be continually consolidated as cycling processes *via* gas coalescence which has been clearly demonstrated in 2D (Figs. 2h & J). Those isolated bubbles will agglomerate horizontally (along with X-axis), leading to formation of gas

channels with an uneven thickness vertically (along with Z-axis). The thickness distribution validated our prior observation, In Fig. 4f the mean thickness of each gas layer ($T_{gas\text{-}middle}$) in the middle region increases from 136.5 to 177.31 µm. At the 100th cycle mark, lots of thin areas (< 105 µm, in blue) are randomly distributed (Fig. 3a). After the 200th cycle, those blue layers were largely replaced by considerably thicker layers (> 180 µm, green and yellow area) as shown in Fig. 3c. The thickest areas (> 230 µm, in red and orange colours) were clearly found towards the middle of sample (i.e., Zone 1-2).

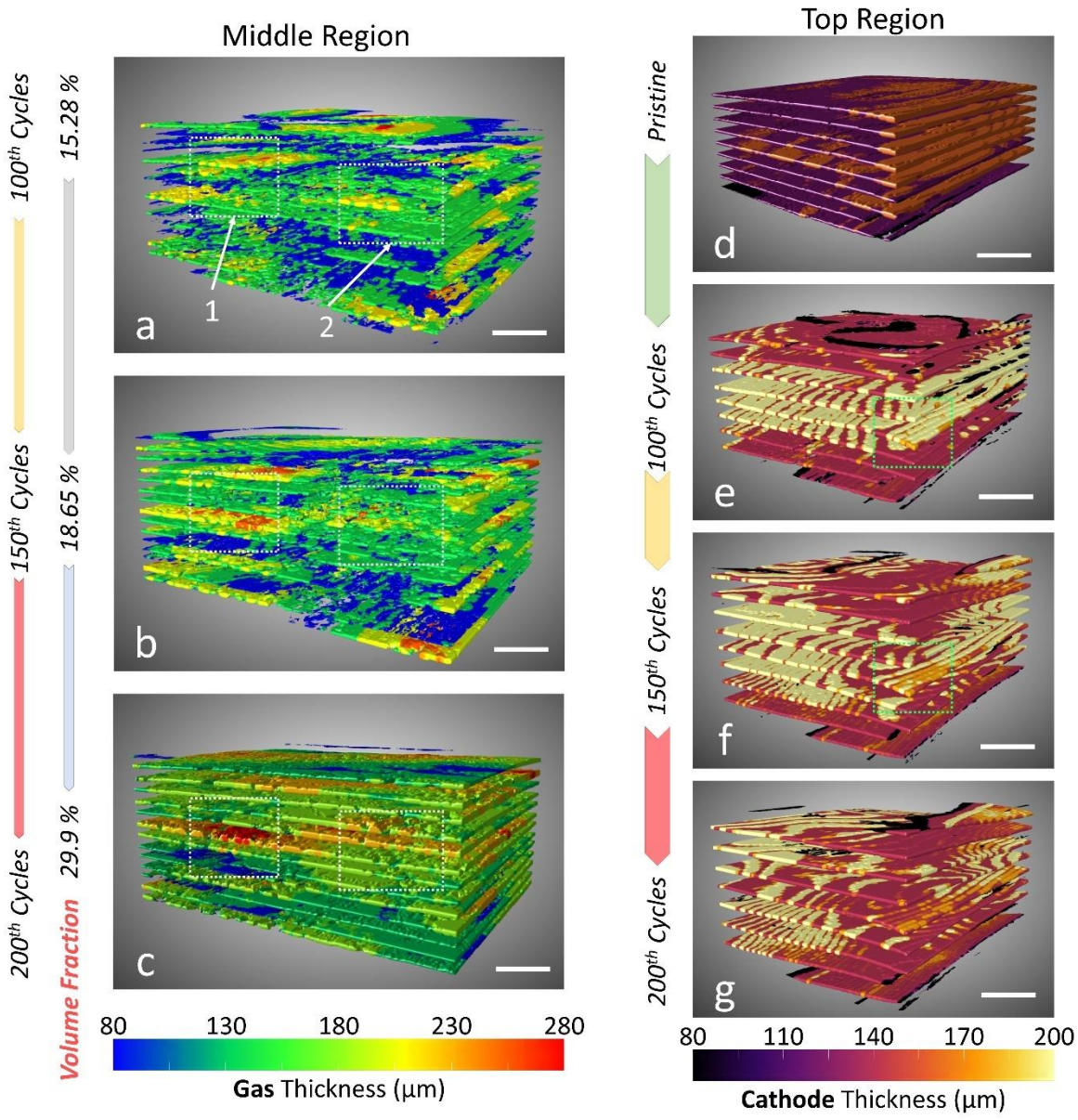

Fig. 3. Time-resolved 3D images of cell morphologies of Li-ion pouch cell before and after various (100th, 150th, and 200th) cycles. The visualization and quantification of (a-c) gas and (d-g) cathodes meso-structures evolution *via* the thickness measurements at middle and top regions, respectively. Scale bars represent 1 mm for all figures.

Similarly, 4D images of gas evolution, extracted at the top and bottom regions (Region i & iii in Fig. S2), are presented in Fig. S5 to demonstrate the non-uniform gas distributions. Unlike the case in the middle region (left column of Fig. 3), under the same cycling conditions we observed lots of large empty zones at the top (i.e., Zone 3-5 in Fig. S5a) and bottom (i.e., Zone 6-7 in Fig. S5d) regions. This suggests that gas has not been produced at this location after 100 cycles. This also implies that the gas formation at both ends of the cell are less significant than in its middle region. Indeed, in Fig. 4b, the initial gas volume (4×10^{10} µm^3) in the middle region is nearly four times higher than those ($\sim1.2\times10^{10}$ µm^3) at both ends. After the 200th cycle, the middle region has the highest gas volume, peaking at $\sim8\times10^{10}$ µm^3 (equivalent to ~80 µL), whereas both ends have similar, low gas volumes of $\sim3.5\times10^{10}$ µm^3. In sum, the average thickness of the gas layer at both ends is usually 20~40 µm thinner than that at the middle region, at the same cycled state (Fig. 4f). Furthermore, X-ray imaging allows us to determine gas volumes for the above three regions, the total experimentally determined gas volume in this cell is above to $\sim1.5\times10^{11}$ µm^3 ($V_{\mathrm{exp}} \geq V_{\mathrm{top}} + V_{\mathrm{mid}} + V_{\mathrm{bot}}$). We have quantified the gas evolution; however, it is difficult to determine if the majority gas is being formed in the centre of the cell due to a higher electrochemical activity, or if it is formed everywhere in the cell but subsequently travels to the centre driven by a pressure gradient. Nevertheless, time-lapse X-ray CT provides an opportunity to measure the cycle-induced thickness change.

It is also well known that the cycle-induced gas evolution plays a role in performance loss [8]. On the one side, it will decrease the electrochemical performance as the sources of gassing are mainly from the electrolyte decomposition and electrode degradation, the evolved gas will lead to structural delamination that increases the cell impedance (see Fig. 1c). On the other side, the accumulation of gas will increase the interior pressure and lead to severe volume expansion (see Fig. 1h), the internal pressure may eventually be released. In a worst scenario this will damage the cell mechanical integrity. If this happens, several highly flammable, toxic products will be released and thermal runaway can result. Hence, there is a pressing need to examine the gas status in the cell to evaluate the SOH of used LIBs. The dynamic, quantitative information relating to gas evolution is difficult (or perhaps impossible) to obtain by other measurements. For example, the measurement of volume change *via* the traditional Archimedes' principle [5, 10, 31, 32] may introduce additional complexity and safety issues due to the requirement to emerge the cell into liquid; moreover, these measurements do not provide local, internal information.

We also present the evolution of cathode structure at the top region in Fig. 3d-g. The morphology shows multiple cathode layers. The cathode volume fraction ($V_{cathode}$) experienced a minor decrease (Fig. 4c) because the gas evolution reaction may happen at the interface between the electrode and electrolyte to produce the gas. Whereas the cathode specific surface area ($S_{cathode}$) was nearly unchanged (fluctuate between 0.021 and 0.025 $\mu m^2/\mu m^3$) as shown in Fig. 4d. The above results may be attributed to the metal-oxide cathode that has a relatively stable structure. Moreover, the mean thickness of cathode ($T_{cathode}$) underwent a minor increase after cycles comparing with gas thickness (T_{gas}). For example, in Fig. 4e, the $T_{cathode\text{-}top}$ at the pristine, 100^{th} and 200^{th} cycle states are 152, 155 and 157 µm respectively, resulting in a total ca. 5 µm expansion. In addition, the cathode structure and

thickness at the middle (left column) and bottom (right column) regions show similar trends in Fig. S6. It should be noted that our electrode thickness values obtained by X-ray tomography (Fig. 4e) are very comparable with the physical measurements by a digital thickness gauge (Fig. S7), demonstrating the accuracy and reliability of X-ray approach. Our disassembled cathode layers were measured to be ca. 147 µm after 50 cycles (ca. 150 µm by X-ray imaging). Furthermore, the local thickness is different from that of the average thickness across the entire region, this local information provides an opportunity to visualise the ROIs (i.e., preferntial degradation areas) in any used cell. This localized heterogeneous electrode thickness could be attributed to the heterogenous current distribution during de-lithiation/lithiation, which may accelerate cell degradation [33]. Interestingly, a uniform thickness distribution (ca. 170 µm) was obtained at the bottom region after the 200th cycle (Fig. S6h). This suggests that the geometric restriction (in our case the walls of the sample holder) may help to achieve a homogeneous reaction at the electrodes, and hence, the electrochemical performance can be improved by applying uniform pressure on the cell [34]. In summary, we propose that the cycle-induced deformation of Li-ion pouch observed is due to the synergistic effect of the thickening of the gas layers and the electrodes. Although the local thickness of electrode materials and gas determines the overall thickness, our result shows the generated gas volume plays a major role in cell bulging. Hence, the volumetric swelling in Li-ion pouch batteries is different from other chemistries, for example Li-S pouch cells which are principally driven by volumetric expansion of the electrodes [15]. Moreover, the development of better electrolyte [35] and electrode materials [36] could mitigate gas generation. Hence, *in-situ* X-ray imaging, in conjunction with other diagnostic techniques [37] such as EIS and acoustics, are vital to further explore degradation mechanisms for pouch cells and help monitor the SOH for safety use.

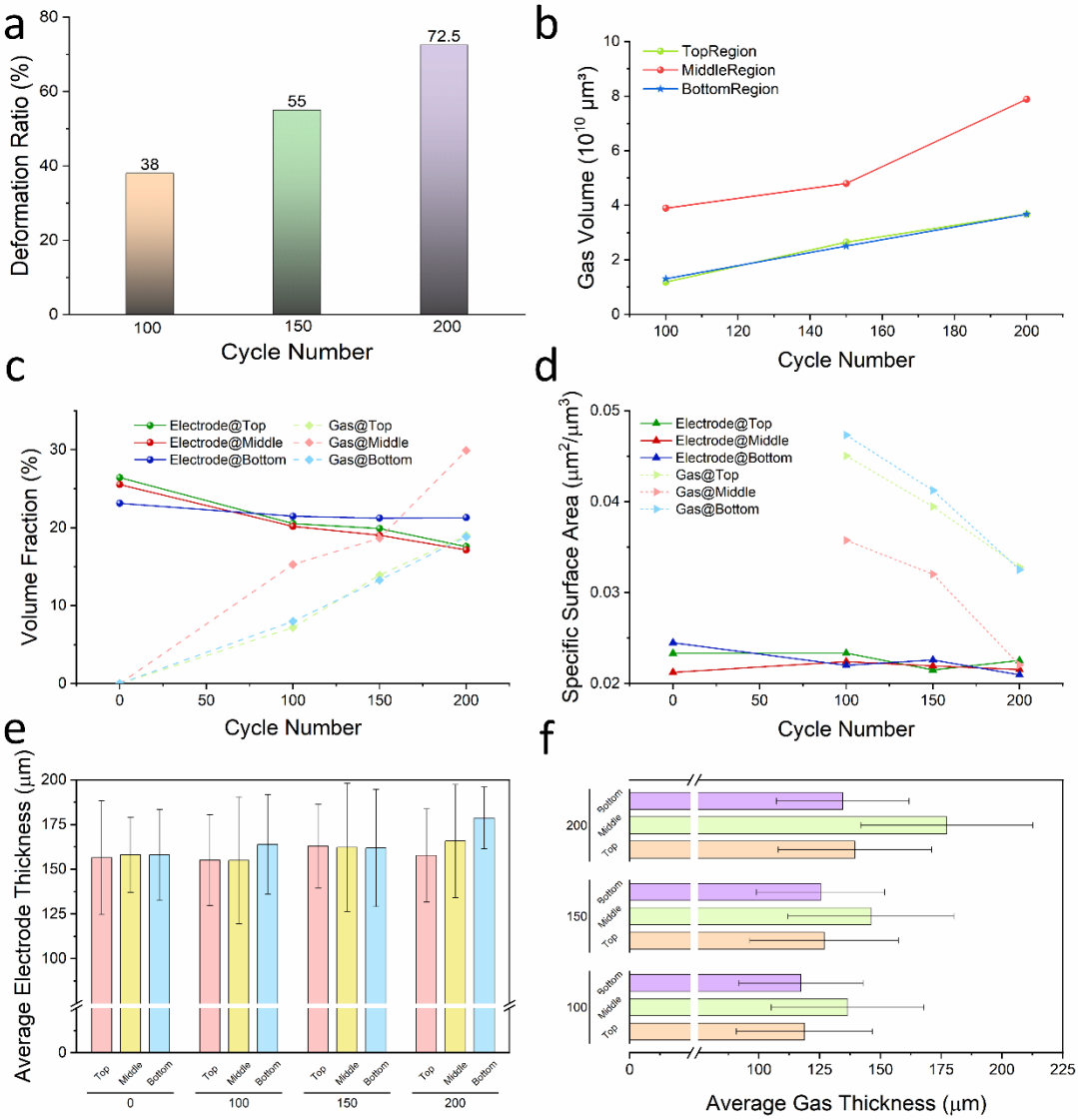

Fig. 4. The quantification of cycle-induced meso-structures evolution at three different regions within Li-ion pouch cell. (a) The cell deformation ratio at X-Y plane after various cycle numbers (100th, 150th, and 200th). (b) The continuous formed gas volumes against the cycle numbers *via* the electrolyte decomposition. Both the cathode and the gas phases (c) volume fraction and (d) specific surface area as a function of cycle numbers. The evolution of average thickness of (e) cathode layers and (f) gas layers before and after 100, 150 and 200 cycles.

4. Conclusion

For the first time, we demonstrate the application of lab-based X-ray tomography to study the cell architecture evolution as a function of cycle numbers for the Li-ion pouch cell, *in-situ*. The large amount of cycle-induced gas formation led to the severe displacement of electrodes

(volume expanded by 72.5%), transfer resistance increases and ultimate capacity fade (drops from 425 to 120 mA h). The gas formation showed a non-uniform distribution, with the volume fraction and average thickness of the gas channels in the middle region being almost double that at both ends of the cell. Furthermore, as the cycles progress the isolated gas bubbles will agglomerate in the horizontal direction and become thicker in the longitudinal direction, resulting the formation of gas layer structure with thickness of 136-177 μm after the 200th cycle. The average gas thickness had a major increase (ca. $20\sim40$ μm), whereas cathode thickness underwent only a minor increase (< 10 μm) after cycling. We therefore propose the deformation of the Li-ion pouch is due to a synergistic effect of the thickening of the gas layers and the electrodes. Time-lapse X-ray tomography enriches our understanding of the electrochemical activities in a real functional Li-ion cell, which may provide practical guidance for designing safer LIBs with higher performance by mitigating the gas formation. Future work will be focused on developing the high-resolution approaches to *operando* studies of the effect of various electrolyte formulation, ageing time, C-rates, and external pressures on the cell architecture.

Acknowledgements

We would like to acknowledge the EPSRC (EP/R020973/1, EP/S018204/1) and The Faraday Institution (EP/S003053/1, FIRG001, FIRG003, FIRG015, The SAFEBATT programme and The ReLiB 2.0 programme) for supporting research in the Electrochemical Innovation Lab. Financial support from UK Research and Innovation (LiS:FAB) and the STFC Batteries Network (ST/R006873/1) are also acknowledged. We acknowledge the assistance from Dr Chun Tan and discussion with Miss Drasti Patel during the investigation. P.R.S acknowledges funding from The Royal Academy of Engineering (CiET1718/59).

Declaration of interests

The authors declare that they have no known competing financial interests or personal relationships that could have appeared to influence the work reported in this paper.

CRediT authorship contribution statement

Wenjia Du: Investigation, Project administration, Methodology, Visualization, Formal analysis, Writing - original draft. **Rhodri E. Owen**: Investigation, Formal analysis, Methodology. **Anmol Jnawali**: Investigation, Formal analysis, Methodology. **Toby P. Neville**: Investigation, Formal analysis. **Francesco Iacoviello**: Investigation, Formal analysis. **Zhenyu Zhang**: Investigation, Formal analysis. **Sebastien Liatard**: Investigation. **Dan J.L. Brett**: Supervision, Writing - review & editing, Funding acquisition. **Paul R. Shearing**: Supervision, Project administration, Validation, Writing - review & editing, Funding acquisition.

References

[1] B. Scrosati, J. Hassoun, Y.-K. Sun, Energy & Environmental Science, 4 (2011) 3287-3295. https://doi.org/10.1039/C1EE01388B

[2] P.R. Shearing, L.R. Johnson, Joule, 4 (2020) 1359-1361.https://doi.org/10.1016/j.joule.2020.06.019.

[3] M.S. Whittingham, Chemical reviews, 104 (2004) 4271-4302. https://doi.org/10.1021/cr020731c.

[4] V. Etacheri, R. Marom, R. Elazari, G. Salitra, D. Aurbach, Energy & Environmental Science, 4 (2011) 3243-3262. https://doi.org/10.1039/C1EE01598B.

[5] K.-Y. Oh, J.B. Siegel, L. Secondo, S.U. Kim, N.A. Samad, J. Qin, D. Anderson, K. Garikipati, A. Knobloch, B.I. Epureanu, C.W. Monroe, A. Stefanopoulou, Journal of Power Sources, 267 (2014) 197-202. https://doi.org/10.1016/j.jpowsour.2014.05.039.

[6] J. Self, C. Aiken, R. Petibon, J. Dahn, Journal of The Electrochemical Society, 162 (2015) A796. https://doi.org/10.1149/2.0081506jes.

[7] D.P. Finegan, M. Scheel, J.B. Robinson, B. Tjaden, I. Hunt, T.J. Mason, J. Millichamp, M. Di Michiel, G.J. Offer, G. Hinds, Nature communications, 6 (2015) 1-10. https://doi.org/10.1038/ncomms7924.

[8] B. Rowden, N. Garcia-Araez, Energy Reports, 6 (2020) 10-18. https://doi.org/10.1016/j.egyr.2020.02.022.

[9] J.-P. Schmiegel, M. Leißing, F. Weddeling, F. Horsthemke, J. Reiter, Q. Fan, S. Nowak, M. Winter, T. Placke, Journal of The Electrochemical Society, 167 (2020) 060516. https://doi.org/10.1149/1945-7111/ab8409.

[10] L. Ellis, J. Allen, L. Thompson, J. Harlow, W. Stone, I. Hill, J. Dahn, Journal of The Electrochemical Society, 164 (2017) A3518. https://doi.org/10.1149/2.0191714jes.

[11] X. Zhang, J. He, J. Zhou, H. Chen, W. Song, D. Fang, Science China Technological Sciences, 64 (2021) 83-90. https://doi.org/10.1007/s11431-020-1709-y.

[12] B. Bitzer, A. Gruhle, Journal of Power Sources, 262 (2014) 297-302. https://doi.org/10.1016/j.jpowsour.2014.03.142.

[13] B. Rieger, S. Schlueter, S.V. Erhard, J. Schmalz, G. Reinhart, A. Jossen, Journal of Energy Storage, 6 (2016) 213-221. https://doi.org/10.1016/j.est.2016.01.006.

[14] P. Leung, C. Moreno, I. Masters, S. Hazra, B. Conde, M. Mohamed, R. Dashwood, R. Bhagat, Journal of Power Sources, 271 (2014) 82-86. https://doi.org/10.1016/j.jpowsour.2014.07.184.

[15] S. Waluś, G. Offer, I. Hunt, Y. Patel, T. Stockley, J. Williams, R. Purkayastha, Energy Storage Materials, 10 (2018) 233-245. https://doi.org/10.1016/j.ensm.2017.05.017.

[16] B. Michalak, H. Sommer, D. Mannes, A. Kaestner, T. Brezesinski, J. Janek, Scientific reports, 5 (2015) 1-9. https://doi.org/10.1038/srep15627.

[17] D. Goers, M. Holzapfel, W. Scheifele, E. Lehmann, P. Vontobel, P. Novák, Journal of Power Sources, 130 (2004) 221-226. https://doi.org/10.1016/j.jpowsour.2003.11.065.

[18] M. Lanz, E. Lehmann, R. Imhof, I. Exnar, P. Novák, Journal of power sources, 101 (2001) 177-181. https://doi.org/10.1016/S0378-7753(01)00706-6.

[19] R.F. Ziesche, T. Arlt, D.P. Finegan, T.M. Heenan, A. Tengattini, D. Baum, N. Kardjilov, H. Markötter, I. Manke, W. Kockelmann, Nature communications, 11 (2020) 1-11. https://doi.org/10.1038/s41467-019-13943-3.

[20] H. Zhou, K. An, S. Allu, S. Pannala, J. Li, H.Z. Bilheux, S.K. Martha, J. Nanda, ACS Energy Letters, 1 (2016) 981-986. https://doi.org/10.1021/acsenergylett.6b00353.

[21] J. Nanda, H. Bilheux, S. Voisin, G.M. Veith, R. Archibald, L. Walker, S. Allu, N.J. Dudney, S. Pannala, The Journal of Physical Chemistry C, 116 (2012) 8401-8408. https://doi.org/10.1021/jp3016003.

[22] V. Yufit, P. Shearing, R. Hamilton, P. Lee, M. Wu, N. Brandon, Electrochemistry Communications, 13 (2011) 608-610. https://doi.org/10.1016/j.elecom.2011.03.022.

[23] P. Pietsch, V. Wood, Annual Review of Materials Research, 47 (2017) 451-479. https://doi.org/10.1146/annurev-matsci-070616-123957.

[24] F. Sun, H. Markötter, I. Manke, A. Hilger, N. Kardjilov, J. Banhart, ACS applied materials & interfaces, 8 (2016) 7156-7164. https://doi.org/10.1021/acsami.6b00708.

[25] J.B. Robinson, M. Pham, M.D. Kok, T.M. Heenan, D.J. Brett, P.R. Shearing, Journal of Power Sources, 444 (2019) 227318. https://doi.org/10.1016/j.jpowsour.2019.227318.
[26] J.B. Robinson, R.E. Owen, M.D. Kok, M. Maier, J. Majasan, M. Braglia, R. Stocker, T. Amietszajew, A.J. Roberts, R. Bhagat, Journal of The Electrochemical Society, 167 (2020) 120530. https://doi.org/10.1149/1945-7111/abb174.
[27] I. Dedigama, P. Angeli, K. Ayers, J. Robinson, P. Shearing, D. Tsaoulidis, D. Brett, International Journal of Hydrogen Energy, 39 (2014) 4468-4482. https://doi.org/10.1016/j.ijhydene.2014.01.026.
[28] M.T. Pham, J.J. Darst, D.P. Finegan, J.B. Robinson, T.M. Heenan, M.D. Kok, F. Iacoviello, R. Owen, W.Q. Walker, O.V. Magdysyuk, Journal of Power Sources, 470 (2020) 228039. https://doi.org/10.1016/j.jpowsour.2020.228039.
[29] N. Otsu, IEEE transactions on systems, man, and cybernetics, 9 (1979) 62-66. 10.1109/TSMC.1979.4310076.
[30] M. Onuki, S. Kinoshita, Y. Sakata, M. Yanagidate, Y. Otake, M. Ue, M. Deguchi, Journal of The Electrochemical Society, 155 (2008) A794. https://doi.org/10.1149/1.2969947.
[31] C. Aiken, J. Xia, D.Y. Wang, D. Stevens, S. Trussler, J. Dahn, Journal of The Electrochemical Society, 161 (2014) A1548. https://doi.org/10.1149/2.0151410jes.
[32] C. Aiken, J. Self, R. Petibon, X. Xia, J. Paulsen, J. Dahn, Journal of The Electrochemical Society, 162 (2015) A760. https://doi.org/10.1149/2.0941504jes.
[33] X. Lu, A. Bertei, D.P. Finegan, C. Tan, S.R. Daemi, J.S. Weaving, K.B. O'Regan, T.M. Heenan, G. Hinds, E. Kendrick, Nature Communications, 11 (2020) 1-13. https://doi.org/10.1038/s41467-020-15811-x.
[34] J. Cannarella, C.B. Arnold, Journal of Power Sources, 245 (2014) 745-751. https://doi.org/10.1016/j.jpowsour.2013.06.165.
[35] A. Wuersig, W. Scheifele, P. Novák, Journal of The Electrochemical Society, 154 (2007) A449. https://doi.org/10.1149/1.2712138.
[36] T.M. Heenan, A. Wade, C. Tan, J.E. Parker, D. Matras, A.S. Leach, J.B. Robinson, A. Llewellyn, A. Dimitrijevic, R. Jervis, Advanced Energy Materials, 10 (2020) 2002655. https://doi.org/10.1002/aenm.202002655.
[37] J.B. Robinson, K. Xi, R.V. Kumar, A.C. Ferrari, H. Au, M.-M. Titirici, A. Parra-Puerto, A. Kucernak, S.D. Fitch, N. Garcia-Araez, Journal of Physics: Energy, 3 (2021) 031501. https://doi.org/10.1088/2515-7655/abdb9a.

Table(s) - provided separately

Table 1. The summarised electro-thermal characteristics of the polymer Li-ion cell.

Parameters	Polymer Li-Ion Cell (PL-402248-2C)
Nominal Capacity (25 °C)	400 mA h
Nominal voltage	3.75
Charge Cut-off Voltage (V)	4.2
Discharge Cut-off Voltage (V)	2.75
Charging Current	0.5 C
Discharge Current	0.5 C
Ambient temperature operation range (°C)	15-60
State of Charge (SOC)	3.75
Cycle Number (when X-ray images taken)	0, 100, 150, 200

Table 2. The electrochemical impedance spectra (EIS) of the 210 mAh Li-ion pouch cell was obtained after 20th and 150th cycle at room temperature of 25 °C. The equivalent circuit is shown in Fig. 1C. EIS carried out by applying to the cell an alternate voltage signal with amplitude of 10 mV within the frequency range from 1 MHz to 0.1 Hz.

Cell Condition	**Equivalent circuit**	**R_i (Ω)**	**R_{c1} (Ω)**	**R_{c2} (Ω)**	**R_c (R_{c1} + R_{c2}) (Ω)**	**W**
After 20 cycles	$R_i(R_{c1}Q_1)(R_{c2}Q_2)W$	72.43×10^{-3}	306.7×10^{-3}	64.51×10^{-3}	371.21×10^{-3}	25.32
After 150 cycles	$R_i(R_{c1}Q_1)(R_{c2}Q_2)W$	58.43×10^{-3}	395.2×10^{-3}	73.60×10^{-3}	468.80×10^{-3}	23.82

Table 3. The X-ray tomographic imaging acquisition parameters.

Scan No	**Cyclic Status**	**State of Charge**	**Resolution (µm)**	**Voltage (kV)**	**Power (W)**	**Exposure time (s)**	**Projection No.**	**FOV**
1	Fresh	3.75	23	140	9.1	1	2089	2028^2
2	100	3.75	23	140	9.1	1	2089	2028^2
3	150	.375	23	140	9.1	1	2089	2028^2
4	200	3.75	23	140	9.1	1	2089	2028^2

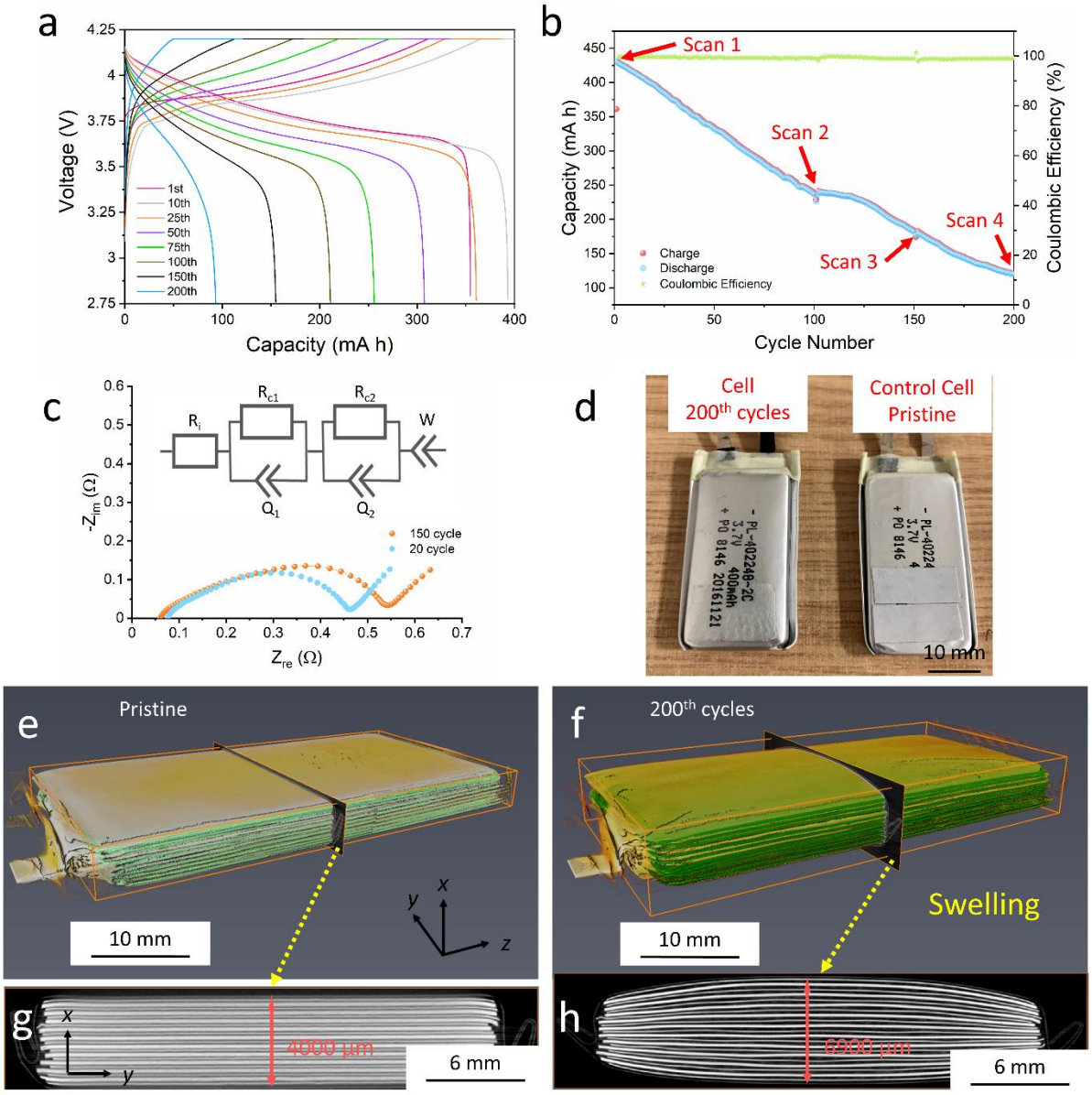

Fig. 1. The room temperature (25 ˚C) electrochmical measurements: (a) the charge-discharge profiles of various cycles (voltage range of 2.75–4.25 V, 1st, 10th, 25th, 50th, 75th, 100th, 150th, and 200th) at a rate of 0.5 C, and (b) the cycling performance for 200 cycles. (c) EIS measurements of the Li-ion pouch cell upon cycling at 0.5 C rate at room temperature, the Nyquist plots are presented for 20th and 150th cycles respectively. (d) The genuine images of the 200th cycles (left) and fresh (right) cells. 3D volume rendering of entire cells and their respective 2D cross-section slices at (e, g) pristine state and (f, h) after 200 cycles. The segmented cathode layers (green) are superimposed with their 3D volumes to highlight the deformation. It should be noted that X-ray tomograms are obtained after the cell is measured at its nominal voltage of 3.75 V.

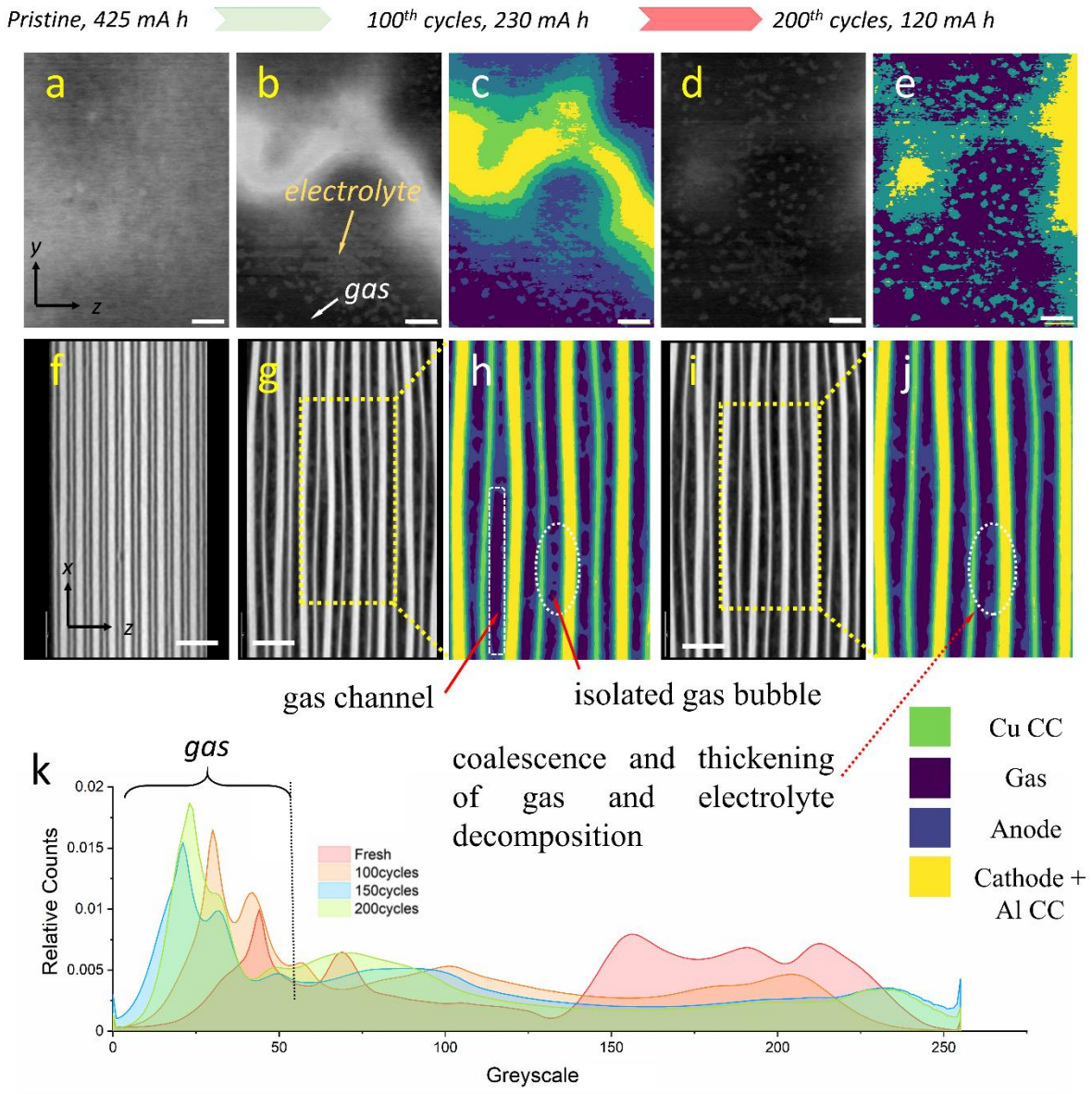

Fig. 2. Time-lapse X-ray tomographic slices of polymer Li-ion pouch cell at the (a, f) pristine, (b, c, g, h) 100th, and (d, e, i, j) 200th cycles, showing the gas evolution and correlative cell deformation. Three sub-volumes (300 × 180 × 400 voxels), included the (a-e) front and (f-j) side view of slices, are extracted from the entire cell volume at the same location. The gas formation, agglomeration, and thickening at mesoscale are highlighted in the enlarge ROI at 100th (h) and 200th (j) cycle. Both images (h & j) are segmented for (g, i) respectively using the multiple Otsu method. The image segmentations (c, e, h, & j) show four labelled phases (green: Cu current collector, yellow: doube cathode layer with Al current collector, blue: electrolyte, and purple: gas). (k) The overlapped X-

ray imaging grayscale histograms of the same cell before and after various cycle numbers. Scale bars are 1 mm for (a-e, f-g, and i).

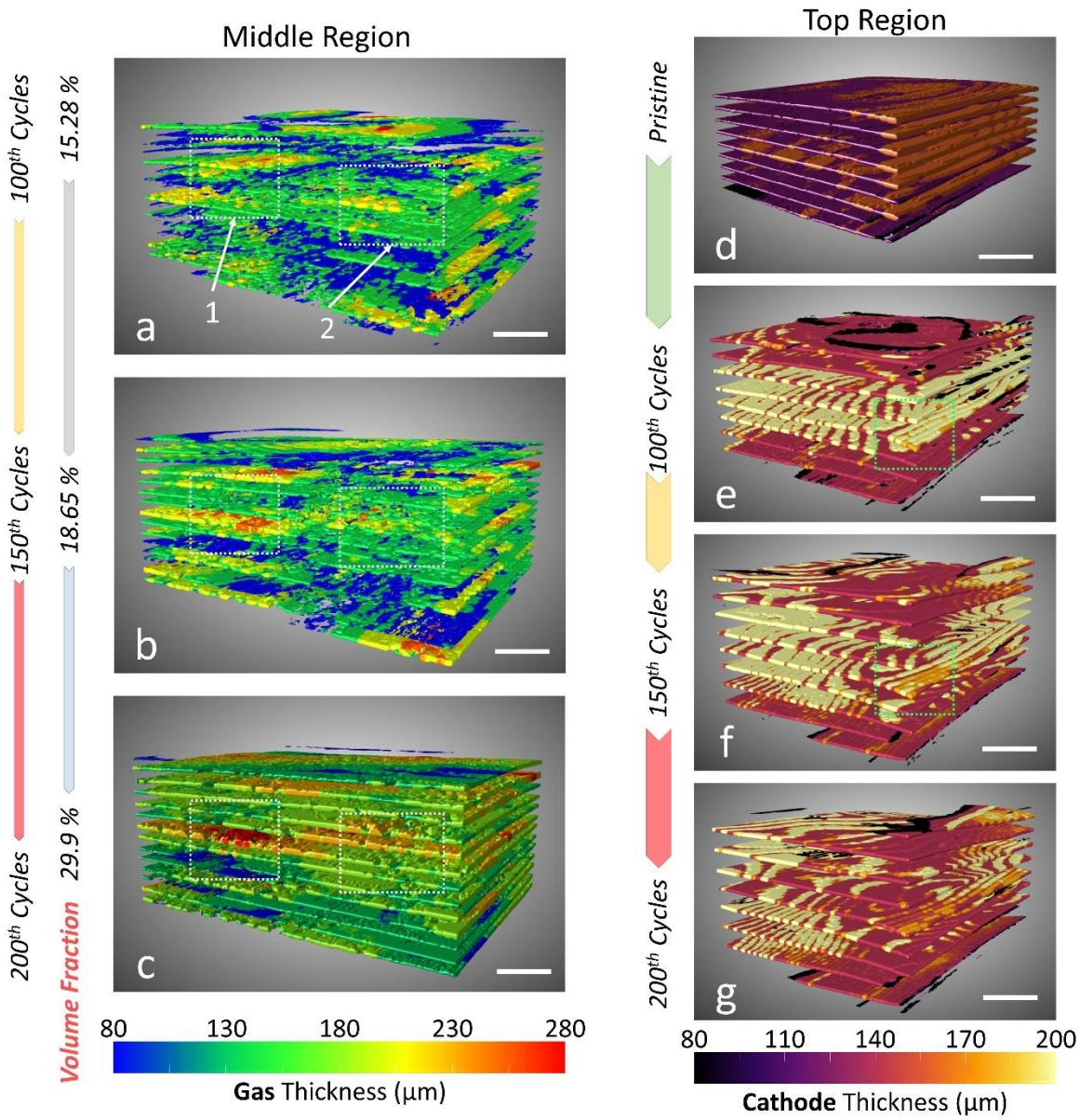

Fig. 3. Time-resolved 3D images of cell morphologies of Li-ion pouch cell before and after various (100th, 150th, and 200th) cycles. The visualization and quantification of (a-c) gas and (d-g) cathodes meso-structures evolution *via* the thickness measurements at middle and top regions, respectively. Scale bars represent 1 mm for all figures.

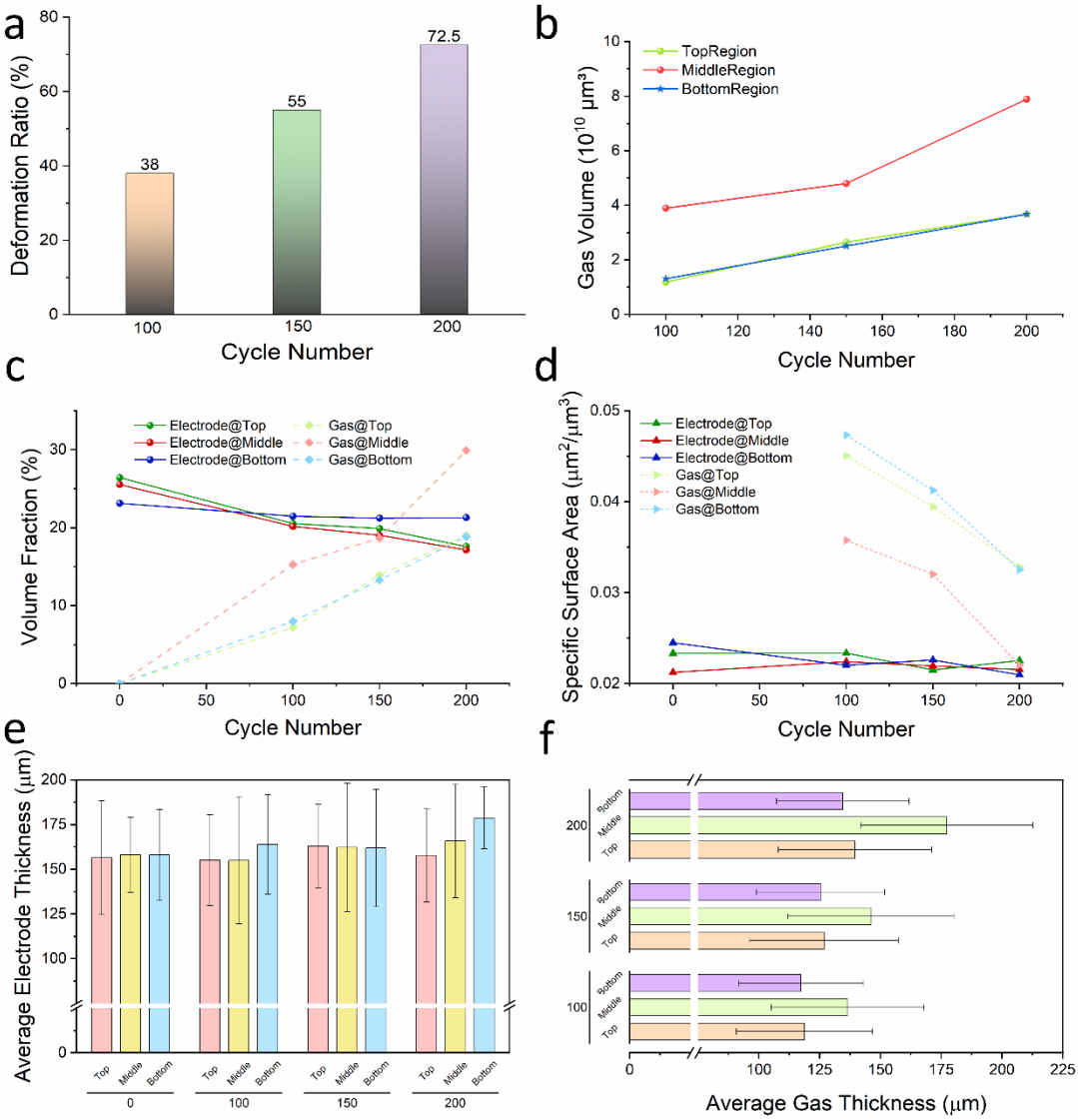

Fig. 4. The quantification of cycle-induced meso-structures evolution at three different regions within Li-ion pouch cell. (a) The cell deformation ratio at X-Y plane after various cycle numbers (100th, 150th, and 200th). (b) The continuous formed gas volumes against the cycle numbers *via* the electrolyte decomposition. Both the cathode and the gas phases (c) volume fraction and (d) specific surface area as a function of cycle numbers. The evolution of average thickness of (e) cathode layers and (f) gas layers before and after 100, 150 and 200 cycles.

Figure Captions

Fig. 1. The room temperature (25 ˚C) electrochmical measurements: (a) the charge-discharge profiles of various cycles (voltage range of 2.75–4.25 V, 1st, 10th, 25th, 50th, 75th, 100th, 150th, and 200th) at a rate of 0.5 C, and (b) the cycling performance for 200 cycles. (c) EIS measurements of the Li-ion pouch cell upon cycling at 0.5 C rate at room temperature, the Nyquist plots are presented for 20th and 150th cycles respectively. (d) The genuine images of the 200th cycles (left) and fresh (right) cells. 3D volume rendering of entire cells and their respective 2D cross-section slices at (e, g) pristine state and (f, h) after 200 cycles. The segmented cathode layers (green) are superimposed with their 3D volumes to highlight the deformation. It should be noted that X-ray tomograms are obtained after the cell is measured at its nominal voltage of 3.75 V.

Fig. 2. Time-lapse X-ray tomographic slices of polymer Li-ion pouch cell at the (a, f) pristine, (b, c, g, h) 100th, and (d, e, i, j) 200th cycles, showing the gas evolution and correlative cell deformation. Three sub-volumes (300 × 180 × 400 voxels), included the (a-e) front and (f-j) side view of slices, are extracted from the entire cell volume at the same location. The gas formation, agglomeration, and thickening at mesoscale are highlighted in the enlarge ROI at 100th (h) and 200th (j) cycle. Both images (h & j) are segmented for (g, i) respectively using the multiple Otsu method. The image segmentations (c, e, h, & j) show four labelled phases (green: Cu current collector, yellow: doube cathode layer with Al current collector, blue: electrolyte, and purple: gas). (k) The overlapped X-ray imaging grayscale histograms of the same cell before and after various cycle numbers. Scale bars are 1 mm for (a-e, f-g, and i).

Fig. 3. Time-resolved 3D images of cell morphologies of Li-ion pouch cell before and after various (100th, 150th, and 200th) cycles. The visualization and quantification of (a-c) gas and (d-g) cathodes meso-structures evolution *via* the thickness measurements at middle and top regions, respectively. Scale bars represent 1 mm for all figures.

Fig. 4. The quantification of cycle-induced meso-structures evolution at three different regions within Li-ion pouch cell. (a) The cell deformation ratio at X-Y plane after various cycle numbers (100th, 150th, and 200th). (b) The continuous formed gas volumes against the cycle numbers *via* the electrolyte decomposition. Both the cathode and the gas phases (c) volume fraction and (d) specific surface area as a function of cycle numbers. The evolution of average thickness of (e) cathode layers and (f) gas layers before and after 100, 150 and 200 cycles.

Table Captions

Table 1. The summarised electro-thermal characteristics of the polymer Li-ion cell.

Table 2. The electrochemical impedance spectra (EIS) of the 210 mAh Li-ion pouch cell was obtained after 20^{th} and 150^{th} cycle at room temperature of 25 °C. The equivalent circuit is shown in Fig. 1C. EIS carried out by applying to the cell an alternate voltage signal with amplitude of 10 mV within the frequency range from 1 MHz to 0.1 Hz.

Table 3. The X-ray tomographic imaging acquisition parameters.

CRediT authorship contribution statement

Wenjia Du: Investigation, Project administration, Methodology, Visualization, Formal analysis, Writing - original draft. **Rhodri E. Owen**: Investigation, Formal analysis, Methodology. **Anmol Jnawali**: Investigation, Formal analysis, Methodology. **Toby P. Neville**: Investigation, Formal analysis. **Francesco Iacoviello**: Investigation, Formal analysis. **Zhenyu Zhang**: Investigation, Formal analysis. **Sebastien Liatard**: Investigation. **Dan J.L. Brett**: Supervision, Writing - review & editing, Funding acquisition. **Paul R. Shearing**: Supervision, Project administration, Validation, Writing - review & editing, Funding acquisition.

Highlights

- 4D X-ray tomographic quantification of the structural evolution in a functioning pouch cell is demonstrated.
- Real-time monitoring of state of health (SOH) by tracking the gas generation and associated coalescence.
- Cell deformation is attributed to a synergistic effect, but the heterogeneous gas distribution plays a major role.

Declaration of interests

☒ The authors declare that they have no known competing financial interests or personal relationships that could have appeared to influence the work reported in this paper.

☐The authors declare the following financial interests/personal relationships which may be considered as potential competing interests:
